ACCSCIENCE PUBLISHING

International Journal of Bioprinting

RESEARCH ARTICLE

Electrohydrodynamically printed microfibrous scaffolds with different pore sizes modulate macrophage polarization and foreign body reaction to enhance bone regeneration

Junzheng Liu[1,2†], **Zijie Meng**[2,3,4,5†], **Jiaming Yu**[6], **Qin Guo**[1], **Jiahao Zhang**[1], **Yulin Wang**[1], **Le Jia**[1], **Jiankang He**[2,4,5*], and **Wei Wang**[1*]

[1]Comprehensive Orthopedics Department, The Second Affiliated Hospital of Xi'an Jiaotong University, Xi'an, Shaanxi, China

[2]State Key Laboratory for Manufacturing Systems Engineering, Xi'an Jiaotong University, Xi'an, Shaanxi, China.

[3]Frontier Institute of Science and Technology, Xi'an Jiaotong University, Xi'an, Shaanxi, China

[4]National Medical Products Administration Key Laboratory for Research and Evaluation of Additive Manufacturing Medical Devices, Xi'an Jiaotong University, Xi'an, Shaanxi, China

[5]State Industry–Education Integration Center for Medical Innovations, Xi'an Jiaotong University, Xi'an, Shaanxi, China

[6]Department of Integrated Traditional Chinese and Western Medicine, Faculty of The First Clinical Medical College, Shaanxi University of Chinese Medicine, Xi'an, Shaanxi, China

Abstract

Foreign body reaction (FBR) is a major obstacle to effective osseointegration in bone defect repair. The pore size of scaffolds is a key determinant of FBR; however, its impact on FBR remains controversial, with limited *in vivo* evidence available. In this study, electrohydrodynamically printed polycaprolactone scaffolds with pore sizes of 100 μm, 200 μm, and 300 μm were fabricated to investigate their effects on macrophage polarization, FBR, and bone regeneration. *In vitro* experiments showed that the 300 μm group promoted M2 polarization of macrophages, reduced tumor necrosis factor-alpha expression (0.71-fold and 0.81-fold relative to the 100 μm and 200 μm groups, respectively), and increased transforming growth factor-beta 1 expression (1.39-fold and 1.19-fold, respectively), thereby enhancing osteogenic gene expression in MC3T3-E1 cells (*Runx2*, *Col1*, and *Ocn*). Finite element analysis and transcriptomics sequencing revealed that pore size-dependent changes in scaffold stiffness modulate Piezo1 activation, influencing macrophage polarization. *In vivo* experiments showed that the 300 μm group exhibited the thinnest fibrous capsule (0.78-fold and 0.79-fold relative to the 100 μm and 200 μm groups, respectively), demonstrated enhanced angiogenesis, and achieved better bone regeneration, with increased bone volume/total volume and bone mineral density. These findings indicate that 300 μm pore-sized scaffolds promote bone regeneration by modulating macrophage polarization and attenuating FBR, providing a basis for optimized scaffold design and clinical translation in bone defect repair.

Keyword: Bone regeneration; Electrohydrodynamic printing; Foreign body reaction; Polarization; Pore size

†These authors contributed equally to this work.

***Corresponding authors:**
Jiankang He
(jiankanghe@mail.xjtu.edu.cn)

Wei Wang
(dr.wangwei@xjtu.edu.cn)

Citation: Liu J, Meng Z, Yu J, *et al.* Electrohydrodynamically printed microfibrous scaffolds with different pore sizes modulate macrophage polarization and foreign body reaction to enhance bone regeneration. *Int J Bioprint*. 2026;12(1):302-322. doi: 10.36922/IJB025410415

Received: October 9, 2025
1st revised: November 7, 2025
2nd revised: November 19, 2025
Accepted: November 19, 2025
Published online: November 19, 2025

Copyright: © 2025 Author(s). This is an Open Access article distributed under the terms of the Creative Commons Attribution License, permitting distribution and reproduction in any medium, provided the original work is properly cited.

Publisher's Note: AccScience Publishing remains neutral with regard to jurisdictional claims in published maps and institutional affiliations.

1. Introduction

Bone defects caused by trauma, infection, inflammation, and tumor resection often exceed the critical size for self-repair.[1–3] These defects often require the implantation of tissue-engineered bone to facilitate bone tissue repair and functional reconstruction.[4,5] Although tissue-engineered bone has significant advantages in treating such defects, its clinical application still faces challenges, among which foreign body reaction (FBR) is the key issue.[6–8] FBR refers to a cascade of complex immune responses initiated by the interaction between an implanted material and host tissue. These responses typically include acute and chronic inflammation, macrophage activation, the formation of multinucleated giant cells, and fibrous capsule development.[9] These reactions hinder bone tissue growth into the implant, which not only reduces the implant's repair capacity but may also ultimately lead to osseointegration failure.[10,11]

Currently, to mitigate FBRs and improve the biocompatibility of implants, researchers are focusing on modifying implants through biological, chemical, and physical means.[12] Biological means focus on loading anti-inflammatory factors (e.g., interleukin [IL]-10 and transforming growth factor-beta [TGF-β]) on the surface of the implants or promoting tissue repair and integration through bioactive coatings (e.g., angiogenic factors and osteogenic coatings).[13,14] Chemical modification, on the other hand, involves adjusting the surface functional groups, hydrophilicity, and degradability of the implants, or releasing drugs or biokines through the degradation process of the implants to precisely modulate the intensity and duration of the immune response.[15,16] Physical means are mainly used to optimize the pore size,[17] shape,[18] and surface morphology of the implants to regulate the adhesion and activation of immune cells, thus reducing the inflammatory response.[19] Notably, physical modifications are intrinsic to the implants and can be seamlessly combined with biological and chemical strategies without introducing toxicity.

Among the physical properties, pore size is a hot topic that has been studied extensively.[20] However, the immune response induced by implants with different pore sizes remains controversial. For example, Jiang *et al*.[21] used a cryoprotectant-assisted freeze-drying method to prepare scaffolds with large (80 μm) and small (30 μm) pore sizes. The experimental results revealed that mouse bone marrow-derived macrophages exhibited a preference for M2 polarization in scaffolds with large pores (80 μm), whereas they were more likely to adopt an M1 phenotype in materials with smaller pores (30 μm). Similarly, Li *et al*.[11] found that scaffolds with a 600 μm pore size more effectively promoted M2 polarization compared to those with a 200 μm pore size. On the other hand, Hady *et al*.[22] fabricated scaffolds with pore sizes of 100 μm and 40 μm using a precise template-based method. Their experimental results demonstrated that the 40 μm scaffold elicited a lower inflammatory response compared to the 100 μm scaffold. The occurrence of two opposite results may be due to the difficulty in establishing a stable immune microenvironment, as it is challenging to achieve precise and controllable dimensions for each pore using these methods.

Emerging additive manufacturing technologies, such as electrohydrodynamic (EHD) printing, have recently provided new solutions for the precise control of pore size.[23,24] EHD printing enables precise control of pore size and fiber arrangement to create a stable immune microenvironment.[25–27] However, there are limited studies on the effect of EHD-printed scaffolds with varying pore sizes on macrophage polarization and their modulation of bone regeneration. To the best of our knowledge, only Tylek *et al*.[28] found that EHD-printed scaffolds with small pore sizes (40 μm) significantly promoted macrophage M2 polarization compared with large pore scaffolds (100 μm), but this study was limited to *in vitro* experiments and did not further explore how macrophage polarization regulates osteogenic differentiation or validate it in an *in vivo* model. Moreover, the underlying mechanisms by which pore size modulates macrophage polarization have yet to be fully elucidated. Notably, *in vivo* studies have indicated that excessively small pores (<100 μm) favor fibroblast differentiation and the infiltration of non-mineralized soft tissue,[29] whereas excessively large pores (>300 μm) may impair cell adhesion, infiltration, and mechanical stability, ultimately compromising bone repair.[30,31]

To address these research gaps, this study utilized EHD printing technology to fabricate polycaprolactone (PCL) scaffolds with pore sizes of 100 μm, 200 μm, and 300 μm, aiming to systematically evaluate their effects on macrophage polarization, FBR, and bone regeneration. The scaffolds were co-cultured with macrophages to assess their impact on macrophage polarization, and the conditioned media from each group were subsequently applied to osteoblast cultures to examine their osteogenic differentiation capacity. Additionally, finite element analysis was conducted to evaluate changes in scaffold stiffness associated with different pore sizes, and transcriptomic sequencing was performed to explore the molecular mechanisms regulating macrophage polarization. A rat subcutaneous implantation model was employed to evaluate scaffold-induced inflammation and FBR. Finally, the effect of pore size on bone regeneration *in vivo* was evaluated using a critical-sized cranial defect model (Figure 1).

2.Materials and methods

2.1. Preparation and characterization of polycaprolactone scaffolds

Medical-grade PCL (molecular weight = 80,000 g/mol, Jinan Daigang Biomaterial Co., Ltd., China) scaffolds were printed using a commercial EHD printing device (Shaanxi Baipusheng Medical Technologies Co., Ltd., China). Three groups of scaffolds were designed, each with a fiber crossing angle of 90° and fiber spacing of 100 µm, 200 µm, and 300 µm, respectively. Specifically, PCL particles were loaded into a glass syringe and maintained at 90°C until a uniform molten phase was formed. During the printing process, a 20-gauge nozzle was used, with a feed rate of 20 µL/h, an applied voltage of 2.4 kV, and a carrier stage speed of 50 mm/s. Throughout the printing process, the

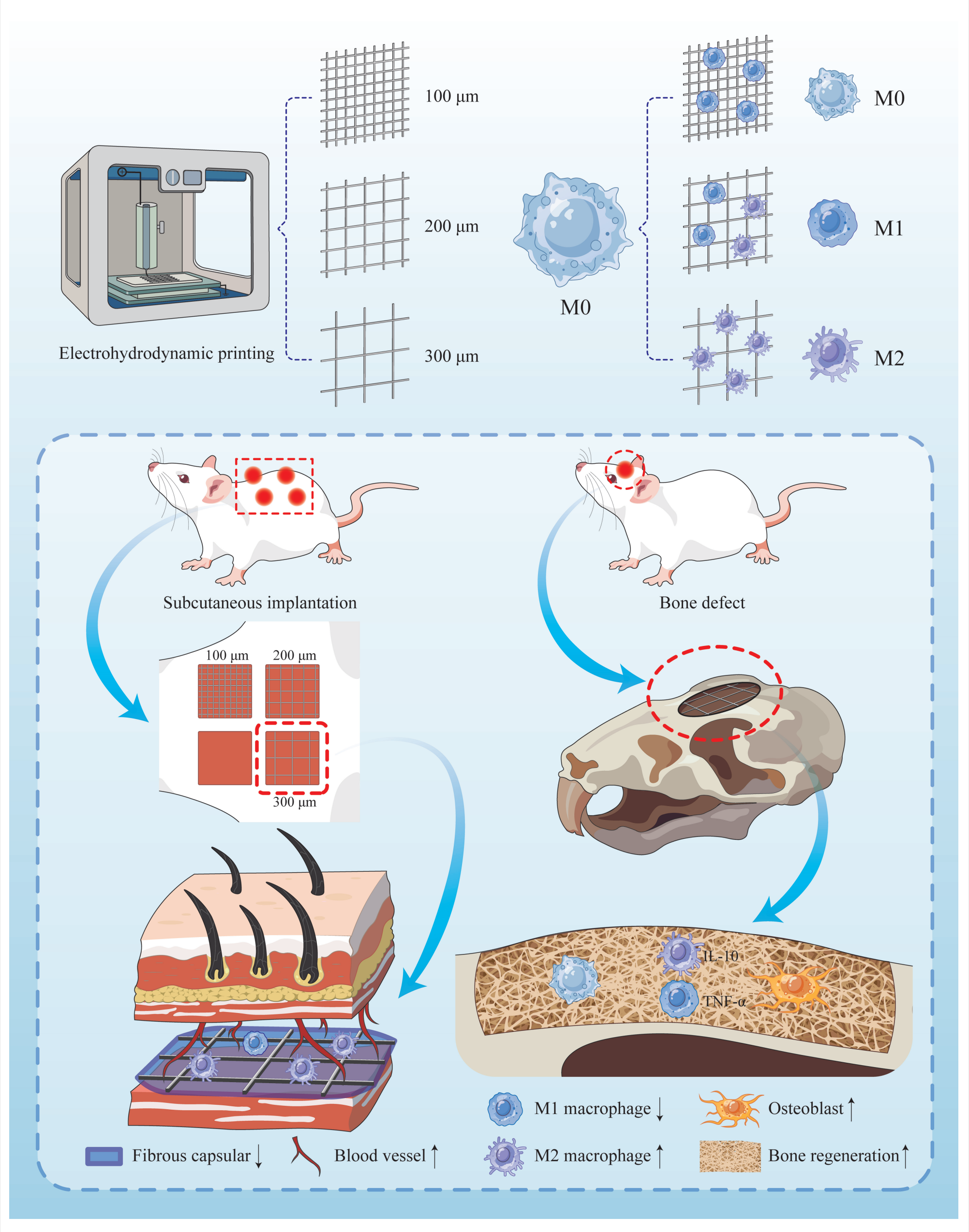

Figure 1. Schematic illustration of electrohydrodynamically printed scaffolds with different pore sizes modulating macrophage polarization and foreign body reaction to promote osteogenesis *in vitro* and *in vivo*. Abbreviations: IL-10, interleukin-10; TNF-α, tumor necrosis factor-alpha.

distance between the nozzle and the collection substrate (indium–tin oxide, glass plate) was maintained at a constant level of 1 mm.[32] The surface morphology and pore architecture of the printed scaffolds were examined using a scanning electron microscope (SEM; SU8010, Hitachi, Japan). The pore sizes of the scaffolds were quantified from SEM micrographs using the ImageJ software (v 1.54h, National Institutes of Health, United States of America [USA]). Tensile tests were then carried out on a universal testing machine (ETM 103A, Jilin Guanteng Automation Technology Co., Ltd.,China) to determine the mechanical performance of the scaffolds.

2.2. Macrophage culture and polarization analysis

RAW264.7 macrophages were maintained in high-glucose Dulbecco's modified medium (DMEM; Gibco, USA) supplemented with 10% fetal bovine serum (Biological Industries, Israel) and 1% penicillin–streptomycin (Gibco, USA). Printed PCL scaffolds were placed in 24-well plates under sterile conditions. After disinfecting the scaffolds by immersing them in 75% ethanol, they were washed three times with sterile phosphate-buffered saline and equilibrated in DMEM medium for 1 h. Subsequently, 1 × 10^5 RAW264.7 cells were seeded onto the scaffold surface and incubated at 37°C in a humidified environment with 5% CO_2.

The effect of different pore-sized scaffolds on macrophage polarization was detected by immunofluorescence staining. Following fixation with 4% paraformaldehyde for 20 min, samples were permeabilized using 0.1% Triton X-100 for 15 min and then blocked with 5% bovine serum albumin for 1 h. Subsequently, primary antibodies, including anti-inducible nitric oxide synthase (iNOS; 1:200, Affinity, Biosciences, USA) and anti-cluster of differentiation 206 (CD206; 1:200, Affinity, Biosciences, USA), were added and incubated overnight at 4°C. After washing, the samples were treated with Alexa Fluor 488- or 594-conjugated secondary antibodies (1:200, Thermo Fisher Scientific, USA) for 1 h at room temperature. Nuclei were then counterstained with 4',6-diamidino-2-phenylindole (DAPI), and images were captured using a confocal laser scanning microscope (A1, Nikon, Japan).

The levels of pro-inflammatory cytokines, including tumor necrosis factor-alpha (TNF-α) and IL-6, as well as anti-inflammatory cytokines, such as IL-4 and IL-10, were quantified using enzyme-linked immunosorbent assay (ELISA) kits (Servicebio, China) following the manufacturer's protocol. Nitric oxide (NO) concentration was measured using the Griess reagent (Beyotime, China). Quantitative real-time polymerase chain reaction (qRT-PCR) was employed to quantify the messenger RNA (mRNA) expression of inflammation-related genes, including *iNos*, *Il1b*, *Tnfa*, *Cd206*, *Tgfb1*, and *Arg1*, in macrophages. Total RNA was isolated from cells using TRIzol reagent (Invitrogen, USA). Complementary DNA was synthesized with a reverse transcription kit (Takara Biotechnology, China). Quantitative amplification was carried out using the SYBR Premix Taq kit (Takara Biotechnology, China), with *Gapdh* as the internal control. The primer sequences used in this study are listed in **Table S1**.

2.3. Osteogenic differentiation assay

To investigate the role of macrophage polarization in regulating osteogenic differentiation, RAW264.7 cells were co-cultured with scaffolds of different pore sizes for 2 days. The collected supernatant was centrifuged at 60 rcf for 5 min and filtered through a 0.22 μm filter to remove any residual cells (Figure S1). The resulting supernatant was mixed with fresh Minimum Essential Medium in a 1:1 ratio to obtain a macrophage-conditioned medium (MCM). MC3T3-E1 osteoblast precursor cells were seeded into 24-well plates at a density of 2 × 10^4 cells per well and cultured in MCM for 14 days.

The marker of early osteogenic differentiation, collagen type I (COL-I), was detected by immunofluorescence staining using anti-COL-I antibody (1:200, Affinity, USA), following the same steps described above. Alkaline phosphatase (ALP) activity and Alizarin Red S (ARS) staining, followed by quantification, were used to assess mid- to late-stage osteogenesis. ALP activity in MC3T3-E1 cells was evaluated using the BCIP/NBT Alkaline Phosphatase Chromogenic Kit (Beyotime, China) on days 7 and 14 of culture. Cells were stained using the ARS kit (Beyotime, China), and a 0.5 N HCl solution containing 5% sodium dodecyl sulfate was added and incubated for 1 h on days 14 and 21 of culture. Absorbance at 405 nm was measured using a microplate reader (Multiskan GO, Thermo Fisher Scientific, USA). Additionally, qRT-PCR was performed to evaluate the expression of genes associated with osteogenesis, including *Col1*, *Alp*, *Runx2*, and *Ocn*. Primer sequences are provided in **Table S1**.

2.4. Simulation analysis model

The relative stiffness of scaffolds with varying pore sizes was assessed using a finite element simulation model based on the simplified beam bending theory.[33] This model calculated the theoretical deflection resulting from a cellular contractile force applied to scaffold fibers at a defined distance from the fiber junction. Based on SEM and fluorescence imaging of cell-seeded scaffolds, the contractile force was assumed to act 30 μm from the fiber intersection. For simplification, it was assumed that each fiber spanned the underlying scaffold layer without deflection or mechanical interference from adjacent fibers.

The total deflection of each group was normalized to the maximum deflection observed in the 300 μm group to allow for relative comparison. To ensure consistency, the applied cellular force was assumed to be constant across all scaffold groups. In addition, since all scaffolds were fabricated using the same material and fiber diameter, both the elastic modulus (E) and the second moment of area (I)—key determinants of bending stiffness—were held constant across groups.

2.5. Transcriptomic sequencing

After 2 days of culture, RAW 264.7 cells were lysed with TRIzol reagent on different scaffold substrates. Total RNA was extracted and sequenced using the Illumina NovaSeq 6000 platform (USA). Differentially expressed genes (DEGs) were identified with criteria of $|\log_2 \text{FoldChange}| > 1$ and $p < 0.05$. Kyoto Encyclopedia of Genes and Genomes (KEGG) pathway enrichment analysis was performed using the online tool at https://www.bioinformatics.com.cn. Key signaling pathways were subsequently validated through immunofluorescence staining and qRT-PCR.[34]

2.6. Subcutaneous implantation in rats

All animal procedures were approved by the Animal Research Committee of Xi'an Jiaotong University and performed in accordance with its guidelines. A total of 24 male Sprague–Dawley (SD) rats, weighing 200 g, were used in this study.

Eight SD rats were used to establish the subcutaneous implantation model. Specifically, the night before the operation, all animals were fasted and were administered 1% pentobarbital (30 mg/kg) for anesthesia in a sterile and clean environment. After satisfactory anesthesia, four longitudinal incisions were made on the back of the rats. After blunt separation, sterile scaffolds were placed in three of the incisions, with the fourth serving as the control. Subsequently, a 4-0 suture was used for suturing. All the animals were in good condition after the operation. To prevent infection, 80,000 units of penicillin were administered within 3 days after surgery. The rats were divided into two groups ($n = 4$ per group) and sacrificed on days 7 (group 1) and 28 (group 2) after implantation. Scaffolds and skin tissues from the incision sites were collected for further study.

2.7. Bone defect model of rats

For the bone defect model, 16 male SD rats were randomly assigned to four groups ($n = 4$ per group). Before the experiment, all animals were acclimatized in the experimental environment for 2 weeks. Food and water were fasted the night before surgery. On the day of surgery, anesthesia was administered with 1% sodium pentobarbital (30 mg/kg) in a sterile and clean environment. After sufficient anesthesia, the rats were shaved at the top of the skull and immobilized. An incision was made along the midline of the head to expose the skull. The defect area was localized according to the anatomical landmarks of the medial canthus and the middle cranial suture. A circular bone defect was precisely induced using an 8 mm-diameter ring drill, taking care to avoid thermal damage. In the experimental groups, an 8 mm-diameter, 0.5 mm-high circular scaffold was placed on the defect area, while the control group received no treatment. The surgical incisions of all animals were subsequently closed layer by layer. Postoperatively, 80,000 units of penicillin were administered intramuscularly daily for 3 days to prevent infection. Rats were euthanized 12 weeks later, and cranial specimens were collected for analysis.

2.8. Micro-computed tomography analysis

The cranial specimens were cleaned and fixed in 10% formalin solution after collection. Subsequently, the samples were analyzed with micro-computed tomography (CT), with an 8 mm-diameter, 2 mm-high cylinder defined as the region of interest (ROI). The scanning parameters were set to a tube voltage of 80 kV and a tube current of 0.06 mA, and a 3D reconstruction analysis was performed. New bone formation was evaluated by calculating the bone volume-to-tissue volume ratio (BV/TV) and bone mineral density (BMD).

2.9. Histological analysis

Subcutaneously implanted animal models were analyzed using hematoxylin–eosin (HE) and toluidine blue (TB) staining. At day 7 post-operation, relative inflammatory cell counts were calculated using the same threshold range in ImageJ. The same statistical analysis was performed for the mast cell counts. The area of two adjacent fibers surrounded by a fibrous capsule was chosen as the ROI, and the cell count was recorded under high magnification. Four ROIs were randomly selected per sample to calculate the density of inflammatory cells. At day 28 post-operation, neovascularization, thickness of the fibrous capsule, and inflammatory cell density were measured from the HE-stained images. The fibrous capsular thickness was calculated using the following equation:

$$\text{Capsular thickness} = \frac{\text{Area enclosed by the blue line} - \text{Area enclosed by the red line}}{\text{Length of the red line}} \tag{1}$$

After micro-CT scanning, all samples were decalcified, followed by paraffin embedding and section preparation. These sections were analyzed by HE and Masson staining to observe new bone formation and collagen fiber distribution. Additionally, immunohistochemical staining was used to measure the expression levels of TNF-α, IL-10, COL-I, and osteocalcin (OCN) at 12 weeks post-surgery to evaluate inflammatory regulation and bone formation. Meanwhile, the M1/M2 phenotypic distribution of macrophages in the defect area was quantified by immunofluorescence staining to further explore the influence of the inflammatory microenvironment on bone repair.

2.10. Statistical analysis

All data are presented as mean ± standard deviation. Prism 9.5.0 (GraphPad Software, USA) was used for statistical analysis. Group differences were analyzed using a two-tailed Student's *t*-test for two groups, and one-way ANOVA followed by Tukey's post-hoc test for comparisons among three or more groups. A $p < 0.05$ was considered statistically significant.

3. Results

3.1. Material characteristics

As shown in Figure 2A, SEM images of PCL scaffolds fabricated by EHD printing showed that the fibers were deposited according to a predetermined trajectory, forming an orthogonal structure with uniform spacing. The measured scaffold pore diameters were 99.83 ± 1.22 µm, 201.40 ± 1.69 µm, and 301.80 ± 1.92 µm, which were very close to the designed target pore diameters of 100 µm, 200 µm, and 300 µm, respectively (Figure 2B).

A universal mechanical tester was used to assess the mechanical properties of the scaffolds. The mechanical properties of the scaffolds showed a decreasing trend with increasing pore diameter (Figure 2C). Specifically, the maximum tensile strength of the 100 µm group was 1.87-fold higher than the 200 µm group and 3.06-fold higher than the 300 µm group (Figure 2D). Although the mechanical properties of the 300 µm groups were lower compared to the other two groups, the mechanical demands of implants for cranial defect repair are relatively low. Previous studies, such as those by Shi *et al.*,[34] have demonstrated that PCL scaffolds with a tensile strength as low as 1 N are sufficient for successful cranial defect repair in rats. Accordingly, the 300 µm group fabricated in this study met the mechanical requirements for cranial defect

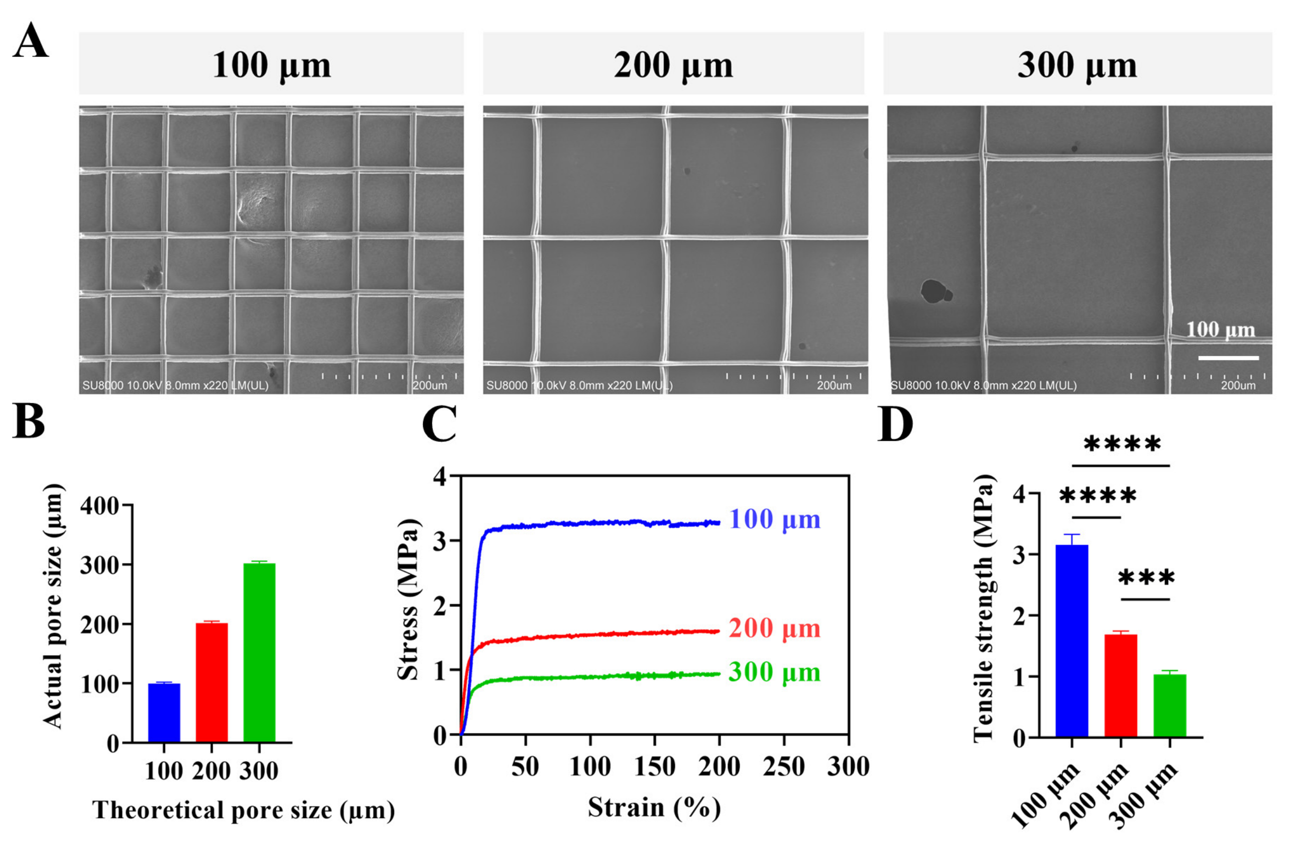

Figure 2. Characterization of microscale fibrous scaffolds with varying pore sizes. (A) Scanning electron microscopy images. Scale bars: 100 µm; magnifications: ×220. (B) Actual pore size measurements. (C) Tensile stress–strain curves. (D) Maximum fracture tensile strength. Notes: $n = 3$; $^{***}p < 0.001$, $^{****}p < 0.0001$.

repair. Altogether, PCL scaffolds with pore sizes of 100 μm, 200 μm, and 300 μm were successfully fabricated in accordance with the intended design specifications.

3.2. Modulation of macrophage polarization by scaffolds with different pore sizes

To evaluate the effects of scaffolds with different pore sizes on macrophage polarization, RAW264.7 macrophages were co-cultured with scaffolds of 100 μm, 200 μm, and 300 μm pore sizes for 2 days. Immunofluorescence staining was used to quantify M1 (iNOS, red) and M2 (CD206, green) marker expression. The intensity of CD206-positive staining was greatest in the 300 μm scaffold group (Figure 3A), with fluorescence intensities that were 1.91-fold and 1.71-fold higher than those observed in the 100 μm and 200 μm groups, respectively (Figure 3C). Conversely, the iNOS-positive fluorescence intensity of the 300 μm scaffold group was the lowest (Figure 3B & D).

To further investigate the effects of different pore sizes on macrophages, the levels of cytokine profiles of RAW264.7 cells were measured by ELISA. The 300 μm group demonstrated the most favorable immunomodulatory profile, characterized by minimal TNF-α/IL-6 and maximal IL-4/IL-10 (Figure 3E & F). Additionally, qRT-PCR analysis confirmed that the 300 μm scaffolds promoted an M2-polarized phenotype, showing downregulated M1 markers (*iNos*, *Il1b*, and *Tnfa*) and upregulated M2 markers (*Cd206*, *Tgfb1*, and *Arg1*) (Figure 3G & H).

Meanwhile, NO is an important effector molecule in macrophages, and differences in its concentration regulate the functional state of macrophages through multiple signaling pathways.[35] The NO concentrations in the 100 μm and 200 μm groups were 2.22-fold and 2.14-fold higher than those in the 300 μm group, respectively (Figure 3I).

3.3. Modulation of the immune microenvironment by scaffolds with different pore sizes to alter osteogenic differentiation

After scaffold implantation *in vivo*, osteoblasts and immune cells were simultaneously recruited to the scaffold surface.[36,37] To mimic the *in vivo* environment and explore the impact of scaffolds with varying pore sizes on immune regulation of osteogenic differentiation, MCM was used to culture MC3T3-E1 pre-osteoblast cells, and osteogenic differentiation markers were assessed at different time points (Figure S1).

In the bone matrix, COL-I, a major component, is secreted by osteoblasts during the early stage and serves as an early indicator of osteogenic differentiation.[38] As shown in Figure 4A, immunofluorescence images showed that the 300 μm group had the highest COL-I deposition, with semi-quantitative analysis revealing levels that were 2.04-fold and 1.90-fold higher than those of the 100 μm and 200 μm groups, respectively (Figure 4D). This trend was confirmed by qRT-PCR results (Figure 4E).

To assess the mid- and late-stage markers of osteogenic differentiation, ALP and ARS staining were conducted.[39] ALP staining is an indicator of early- to mid-stage osteogenic differentiation. At days 7 and 14, the staining image of the 300 μm group showed the highest staining intensity (Figure 4B). Quantitative analysis of ALP activity also confirmed that the 300 μm group had the highest ALP activity (Figure 4F). Similarly, ARS staining reflects calcium deposition, which is considered a marker of late osteogenesis. Compared with other groups, calcium deposition was more extensive and staining intensity was higher in the 300 μm group (Figure 4C). Quantitative analysis of ARS staining supported this finding (Figure 4G).

Additionally, the expression of key osteogenic genes, including *Alp*, *Runx2*, and *Ocn*, was analyzed. The results demonstrated that the expression levels of these genes were consistently highest in the 300 μm group, both at day 7 and day 14 (Figure 4H & I). Notably, after 14 days of culture, these gene expression levels in the 300 μm group were more than double those in the 100 μm group. These results indicate that pore size can alter the immune microenvironment, thereby affecting osteogenesis, with the 300 μm group showing the largest osteogenic effect.

3.4. Simulation and transcriptomic analysis of scaffolds with different pore sizes

To elucidate the potential mechanisms underlying the regulation of macrophage polarization by different pore sizes, simulation analysis and transcriptomic sequencing were performed to examine gene expression differences between groups.

Previous studies, including that by Xu *et al.*,[40] have demonstrated that high scaffold stiffness promotes M1 polarization of macrophages and enhances the secretion of pro-inflammatory cytokines. Accordingly, we constructed a simulation model to investigate how the pore size affects the local stiffness at the cell–scaffold interface. As shown in Figure 5A and B, the scaffold with a 100 μm pore size exhibited markedly increased local fiber bending stiffness. At the microstructural level, fibers spanned the gaps between the underlying support fibers, and the effective span length depended on the interlayer pore size, directly influencing fiber bending behavior. In scaffolds with a 100 μm pore size, the shortest support distance between fiber joints under a given unit load resulted in the smallest maximum deflection, indicating higher local structural

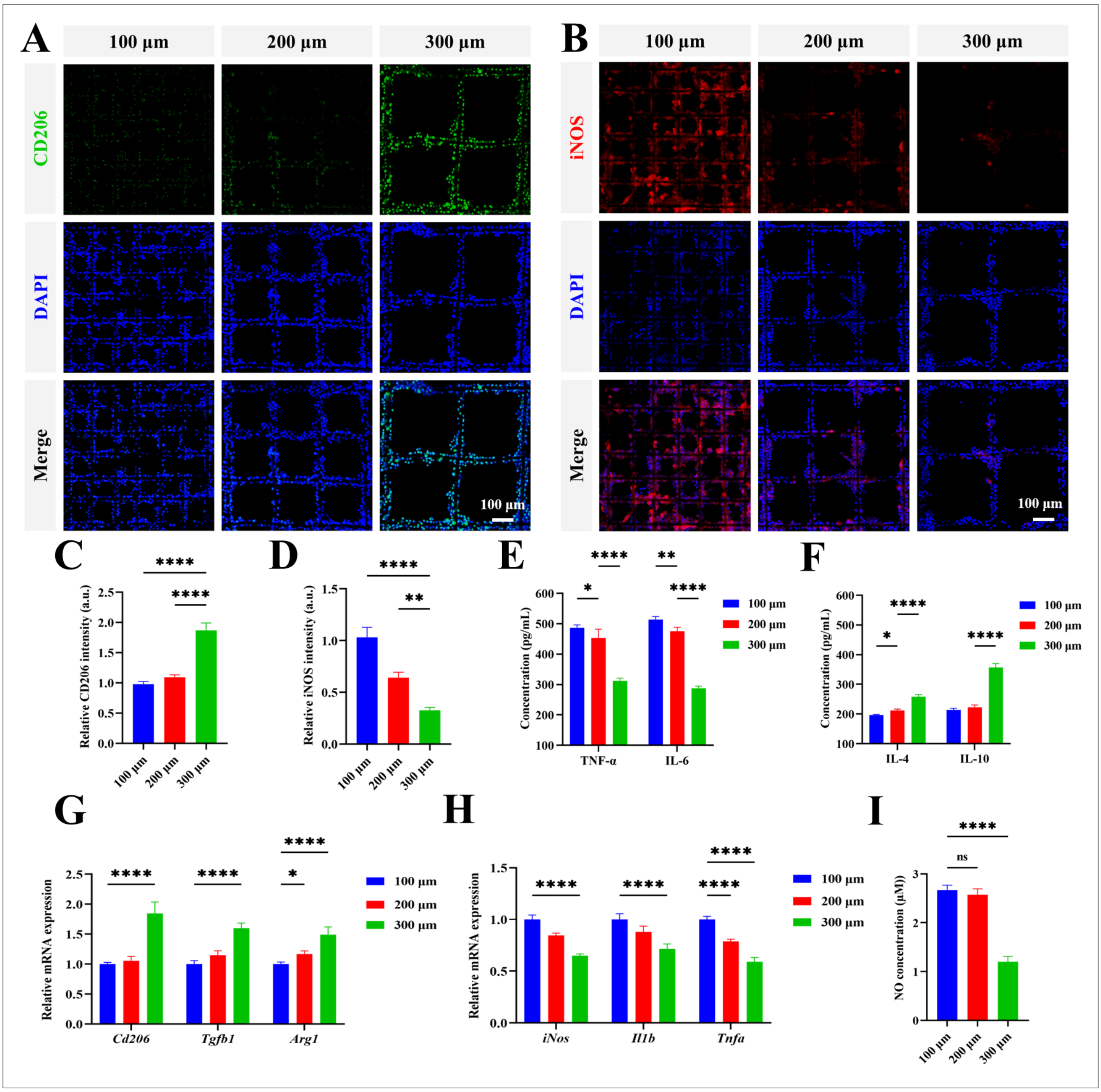

Figure 3. Modulation of macrophage polarization by scaffolds with different pore sizes. Immunofluorescence staining of (A) CD206 and (B) iNOS. Scale bars: 100 μm; magnifications: ×30. Semi-quantitative analysis of (C) CD206 and (D) iNOS. (E) Concentrations of TNF-α and IL-6. (F) Concentrations of IL-4 and IL-10. (G) Gene expression levels of *Cd206*, *Tgfb1*, and *Arg1*. (H) Gene expression levels of *iNos*, *Il1b*, and *Tnfa*. (I) Concentrations of NO. Notes: *n* = 3; $^*p < 0.05$, $^{**}p < 0.01$, $^{****}p < 0.0001$. Abbreviations: NO: CD206, cluster of differentiation 206; IL, interleukin; iNOS, inducible nitric oxide synthase; mRNA, messenger RNA, nitric oxide; TNF-α, tumor necrosis factor-alpha; ns, non-significant.

stiffness. For example, at a point 15 μm away from the fiber junction, simulation results showed that the local bending stiffness of the 100 μm group was approximately 4.10-fold higher than that of the 200 μm group, and 9.28-fold higher than that of the 300 μm group. Moreover, as the distance from the fiber intersection increased, the difference in local stiffness became more pronounced.

To further investigate the impact of local stiffness on macrophage polarization, transcriptomic sequencing analysis was performed. Compared with the 100 μm

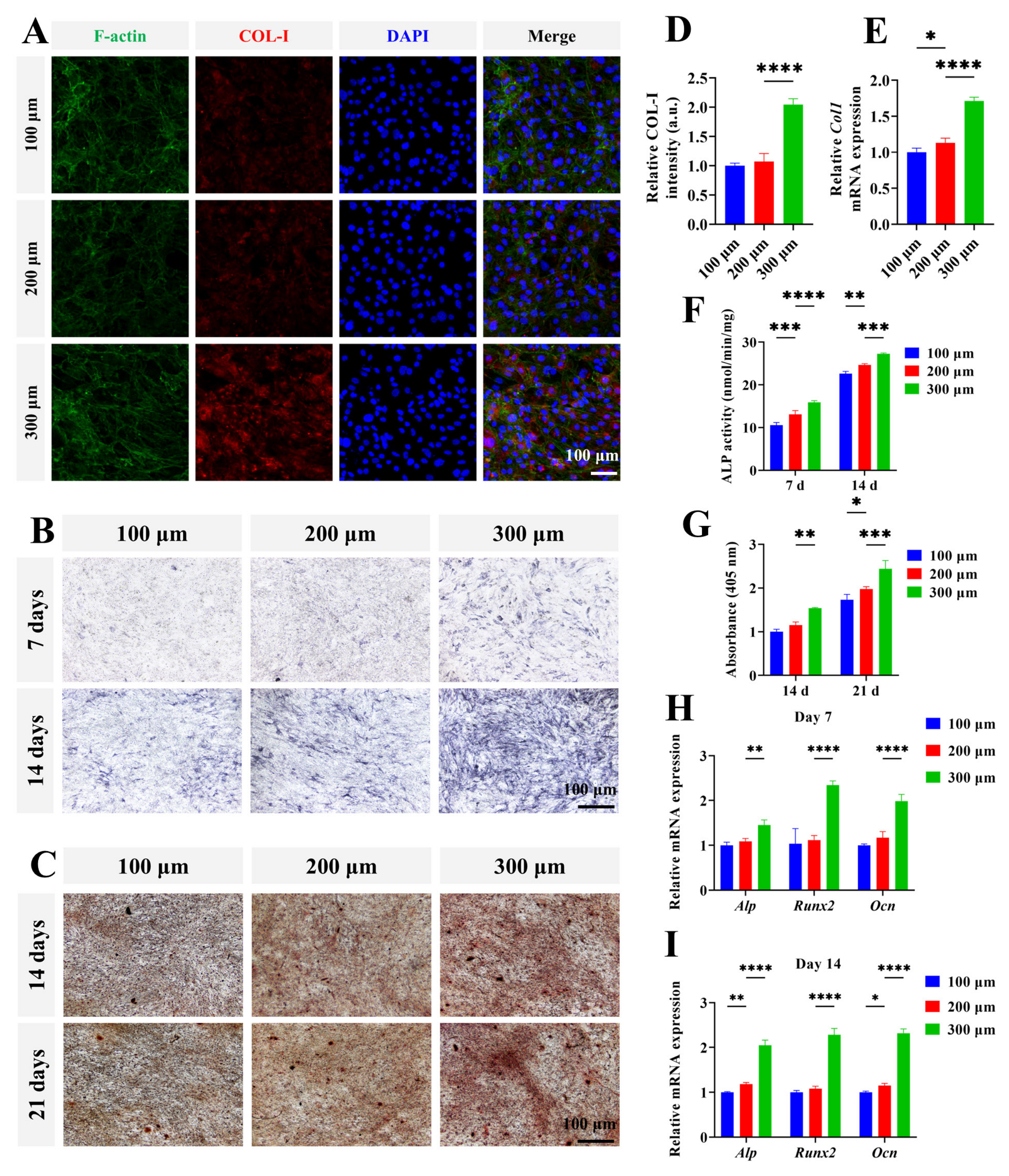

Figure 4. Scaffolds with different pore sizes modulate the immune microenvironment to affect osteogenic differentiation. (A) Immunofluorescence staining of COL-I. Scale bars: 100 µm; magnifications: ×40 . (B) ALP staining images at 7 days and 14 days. Scale bars: 100 µm; magnifications: ×60. (C) ARS staining images at 14 days and 21 days. Scale bars: 100 µm; magnifications: ×60 . (D) Semi-quantitative analysis of COL-I. (E) Gene expression levels of *Col1*. (F) Determination of ALP activity. (G) Quantitative analysis of the ARS. Gene expression levels of *Alp*, *Runx2*, and *Ocn* at (H) day 7 and (I) day 14. Notes: $n = 3$; $^{*}p < 0.05$, $^{**}p < 0.01$, $^{***}P < 0.001$, $^{****}p < 0.0001$. Abbreviations: ALP, alkaline phosphatase; ARS, alizarin Red S; COL-I, collagen type I; DAPI, 4',6-diamidino-2-phenylindole; mRNA, messenger RNA.

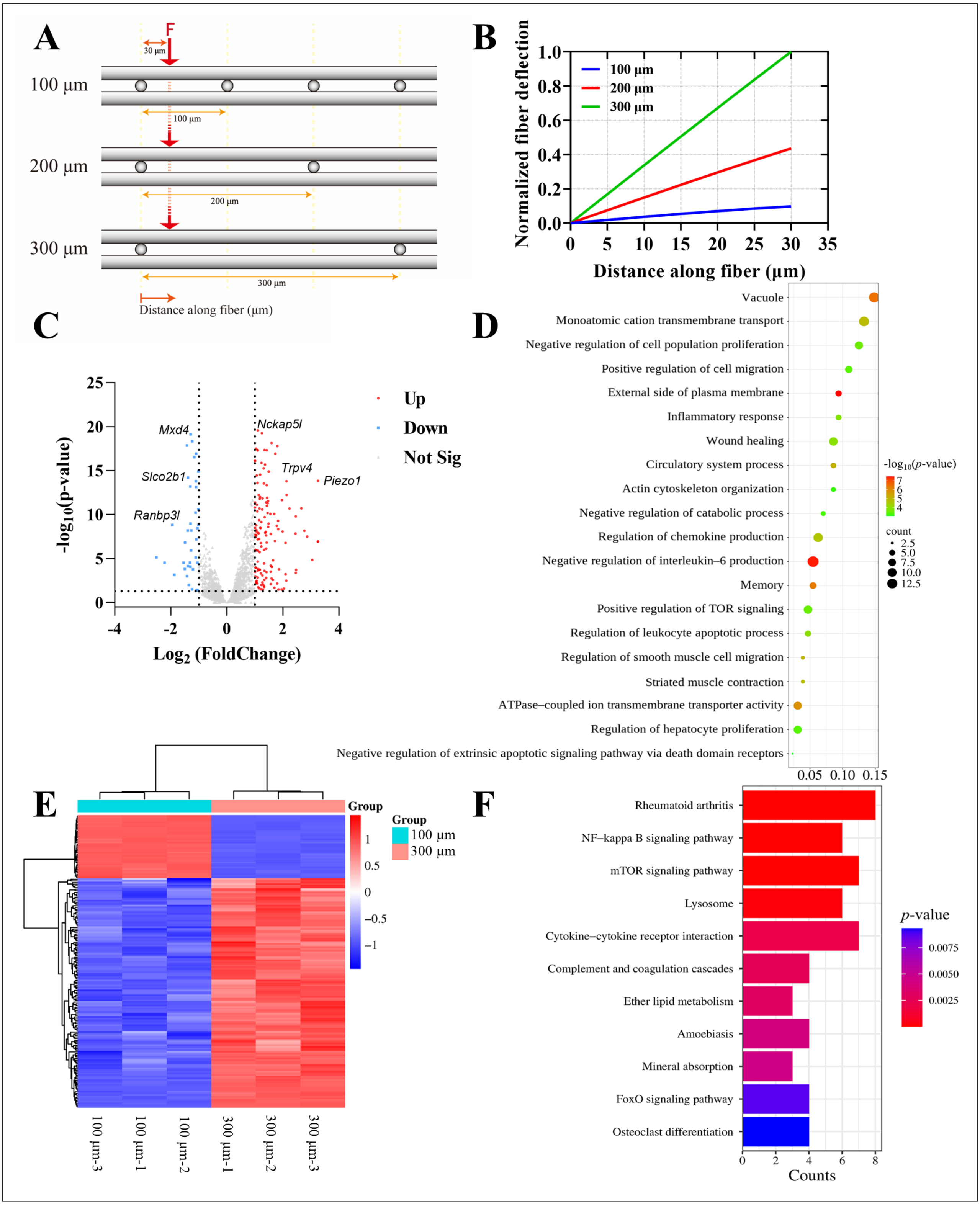

Figure 5. Simulation and transcriptomic analysis of scaffolds with different pore sizes. (A) Analysis model of relative stiffness. (B) Relative deflection. (C) Volcano plot, (D) gene ontology enrichment analysis, (E) heatmap, and (F) KEGG pathway enrichment analysis of differentially expressed genes between the 100 μm and 300 μm groups. Abbreviations: KEGG: Kyoto Encyclopedia of Genes and Genomes; mTOR, mammalian target of rapamycin; TOR, target of rapamycin.

group, the 300 μm group exhibited 138 upregulated and 38 downregulated DEGs (Figure 5C & E). These DEGs were subsequently subjected to gene ontology enrichment analysis, which identifies overrepresented functional categories among a set of genes. As shown in Figure 5D, these DEGs were predominantly enriched in pathways related to the cytoskeleton and ATP-dependent ion transmembrane transporter activity. Additionally, KEGG pathway analysis was conducted to investigate the potential functional implications of these DEGs (Figure 5F). The results indicated that these DEGs may be involved in signaling pathways such as mammalian target of rapamycin and nuclear factor-kappa B, both of which are known downstream targets of the mechanosensitive ion channel Piezo1, which plays a crucial role in converting mechanical stimuli into biochemical signals.[41]

3.5. Modulation of Piezo1 expression and macrophage polarization by scaffolds with varying pore sizes

To verify whether scaffolds with different pore sizes regulate macrophage polarization through Piezo1 activation, immunofluorescence staining and qRT-PCR were conducted. The immunofluorescence results revealed that macrophages cultured on the 300 μm group exhibited significantly higher Piezo1 fluorescence intensity compared to those on the 100 μm and 200 μm groups (Figure 6A & B). Consistently, semi-quantitative fluorescence analysis and qRT-PCR collectively demonstrated the most pronounced Piezo1 expression in the 300 μm group (Figure 6C).

To further validate the role of Piezo1, macrophages cultured on the 300 μm group were treated with small interfering RNA (siRNA)-mediated knockdown and the Piezo1-specific inhibitor GsMTx4 to suppress Piezo1 expression. Both siRNA transfection and GsMTx4 treatment significantly reduced Piezo1 protein expression compared to the untreated control group (Figure 6D).

Subsequently, the polarization status of macrophages was assessed following Piezo1 inhibition. As shown in Figure 6E, the expression of M2 macrophage polarization markers was markedly decreased in the Piezo1-suppressed groups relative to the controls. These findings suggest that Piezo1 may regulate macrophage polarization by modulating the cellular response to mechanical cues, particularly affecting the transition toward the anti-inflammatory M2 phenotype.

Collectively, these results demonstrate that scaffold pore size can influence macrophage polarization by altering the mechanical stiffness of the material. Further mechanistic investigation revealed that the upregulation of the mechanosensitive ion channel Piezo1 underlies this process. Through Piezo1 activation, macrophages are able to detect variations in scaffold stiffness, thereby modulating their polarization states accordingly.

3.6. Assessment of the foreign body reaction in a rat subcutaneous implantation model

The results of *in vitro* experiments showed that a 300 μm pore size could further promote macrophage M2 polarization, improving the osteogenic immune microenvironment. To further evaluate the immune responses of scaffolds with different pore sizes *in vivo*, we implanted the scaffolds subcutaneously in rats and assessed the acute and chronic inflammatory responses. After 7 days of implantation *in vivo*, histological evaluation employing HE and TB staining was performed to detect acute inflammation. The HE staining demonstrated a significant reduction in inflammatory cells on the surfaces of the 300 μm scaffolds compared to the other two groups (Figure 7A & F). Notably, dense clusters of foreign body giant cells (FBGCs), indicative of FBR, were observed at the interface between scaffolds and host tissues in the 100 μm group. The TB staining further demonstrated that the number of mast cells, which are markers of acute inflammation, was significantly higher in the 100 μm and 200 μm groups than in the 300 μm group (Figure 7C & G). These findings indicate that the acute inflammatory response was considerably milder in the 300 μm group.

To assess the chronic inflammatory response, the HE staining was performed at 28 days post-implantation. The 300 μm group exhibited significant neovascularization within the scaffold (Figure 7B), suggesting enhanced tissue integration and remodeling. Furthermore, the number of inflammatory cells was markedly lower in the 300 μm group compared to the 100 μm and 200 μm groups (Figure 7E). The thickness of the fibrous capsule at the scaffold–host tissue interface, an indicator of chronic inflammation and biocompatibility, was also evaluated. Compared with other groups, the 300 μm group showed the thinnest fibrous capsule (Figure 7D & H), further indicating a more favorable immune response and reduced FBR.

3.7. Effect of scaffolds with different pore sizes on macrophage phenotypic switching in a bone defect model

Macrophages play a pivotal role in bone repair and reconstruction by mediating the initial inflammatory response and secreting various factors that regulate osteogenesis and osteoblastogenesis.[42] They are essential for the process of osseointegration following foreign body implantation.[43] Our results have demonstrated that a 300 μm pore size effectively promotes macrophage M2 polarization *in vitro*.

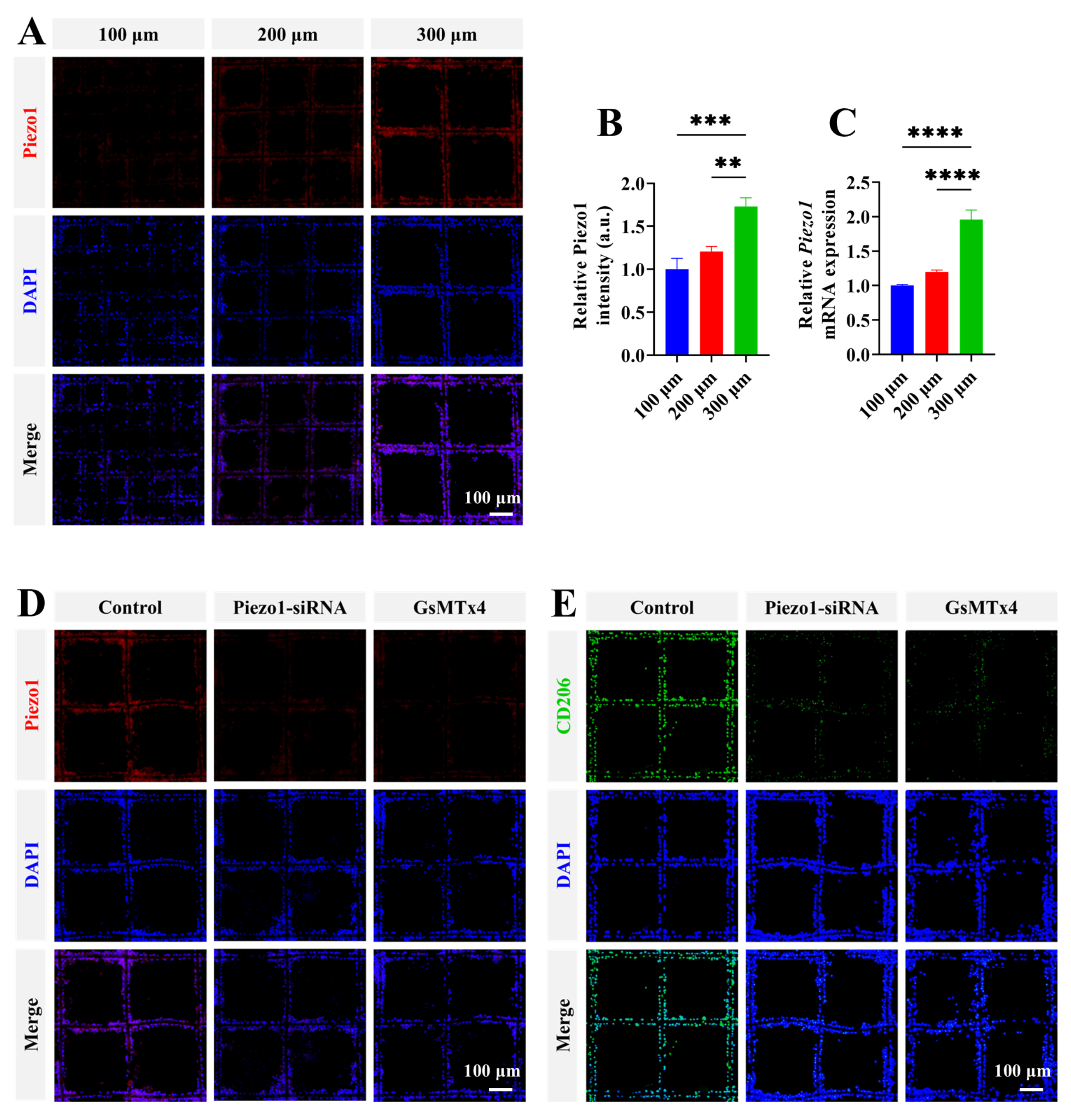

Figure 6. Scaffold pore size modulates Piezo1 expression and regulates macrophage polarization. (A) Immunofluorescence staining (scale bars: 100 µm; magnifications: ×30) and (B) semi-quantitative analysis of Piezo1 in the three groups of scaffolds. (C) Gene expression level of *Piezo1*. Immunofluorescence images of (D) Piezo1 and (F) CD206 expressions in macrophages in the 300 µm group after siRNA knockdown and GsMTx4 treatment. Scale bars: 100 µm; magnifications: ×30. Notes: *n* = 3; $^{**}p < 0.01$, $^{***}p < 0.001$, $^{****}p < 0.0001$. Abbreviations: DAPI, 4',6-diamidino-2-phenylindole; siRNA, small interfering RNA.

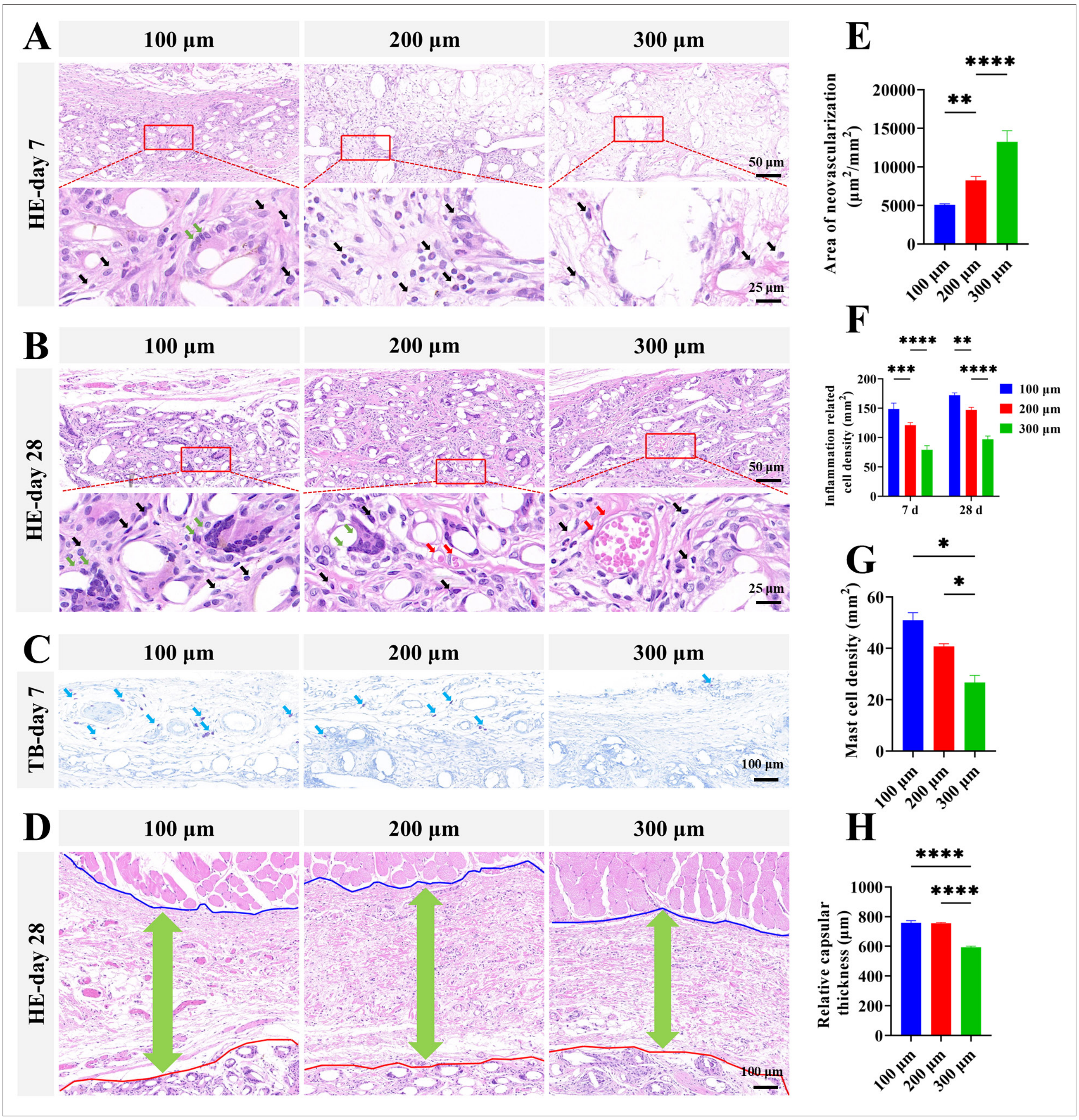

Figure 7. Assessment of the effects of scaffolds with varying pore sizes on foreign body reaction in the rat subcutaneous implantation model *in vivo*. HE staining images at (A) day 7 and (B) day 28. Scale bars: (top) 50 µm, (bottom) 25 µm; magnifications: (top) ×80, (bottom) ×160. (C) TB staining images at day 7. Scale bars: 100 µm; magnifications: ×40. (D) Fibrous capsule measurements at day 28. Scale bars: 100 µm; magnifications: ×40. Statistical analyses of the (E) neovascularization, (F) inflammatory cell density, (G) mast cell density, and (H) Fibrous capsule thickness measurements. Notes: Black arrows indicate inflammatory cells; green arrows indicate FBGC; red arrows indicate neovascularization; blue arrows indicate mast cells; $n = 4$; $^*p < 0.05$, $^{**}p < 0.01$, $^{***}p < 0.001$, $^{****}p < 0.0001$. Abbreviations: FBGC, foreign body giant cells; HE, hematoxylin–eosin; TB, toluidine blue.

To further investigate this phenomenon, we conducted *in vivo* experiments using a rat cranial bone defect model to examine the influence of scaffold pore size on macrophage phenotypic transition. Immunofluorescence analysis was performed to evaluate macrophage phenotypes following implantation of scaffolds with three different pore sizes (100 μm, 200 μm, and 300 μm) into the bone defect site. CD163 was used as a marker for M2 macrophages, while iNOS was used to label M1 macrophages. The results showed that the 300 μm group had the highest green fluorescence intensity, indicating that it had the highest number of M2 macrophages (Figure 8A). In contrast, the 100 μm group showed the strongest red fluorescence intensity, indicating the highest M1 macrophage density, whereas the 300 μm group showed the weakest. Further analysis of the M2/M1 macrophage ratio revealed that the 300 μm group achieved a ratio of 1.64, which was 2.52-fold and 1.51-fold higher than that of the 100 μm and 200 μm groups, respectively (Figure 8C).

Additionally, immunohistochemical staining was employed to assess the deposition of the pro-inflammatory cytokine TNF-α and the anti-inflammatory cytokine IL-10 in each group. Compared with the 100 μm and 200 μm groups, the 300 μm group showed a significant decrease in TNF-α deposition and a significant increase in IL-10 deposition (Figure 8B, D, & E).

3.8. Bone regeneration in a rat cranial defect model treated with scaffolds of varying pore sizes

To investigate the effects of scaffolds with different pore sizes on osteogenesis after modulating the immune microenvironment, we conducted a series of *in vivo* experiments using a cranial defect model. Micro-CT analysis was first performed on skull specimens implanted with scaffolds of varying pore sizes. The osteogenic capacity, as determined by 3D reconstruction, was markedly superior in all scaffold groups relative to the scaffold-free control. Among them, the 300 μm group exhibited the highest volume of newly formed bone, although the difference was not visually striking (Figure 9A). Quantitative confirmation was provided by 2D sagittal CT images, which identified the least residual bone defect in the 300 μm group (Figure 9B).

To quantify bone formation, histomorphometric parameters, including BV/TV and BMD, were measured within the bone defect region. Micro-CT analysis showed that the 300 μm group had significantly higher BV/TV and BMD compared to the other groups. This aligns with the quantitative nature of these measurements, despite the relatively subtle visual differences among the reconstructed images (Figure 9C & D).

Histological analyses were conducted using the HE staining and Masson's trichrome staining to assess new bone formation and maturation.[44] The HE staining results revealed that the control group exhibited minimal new bone formation, whereas the 300 μm group had the largest area of newly formed bone and the smallest residual defect length (Figure 9G). The Masson's trichrome staining results showed that the 300 μm group had the highest bone tissue maturity, characterized by dense collagen deposition and regular bone plate structure (Figure 9H).

Additionally, the deposition of COL-I and OCN, key markers of bone formation and maturation, was assessed. Compared to the control group, the 100 μm group, and the 200 μm group, the 300 μm group showed significantly more COL-I and OCN deposition (Figure 9E, F, & I). These findings suggest that scaffolds with a 300 μm pore size provide an optimal microenvironment for promoting osteogenesis and bone maturation *in vivo*. This is likely achieved through enhanced modulation of the immune microenvironment, highlighting the potential of 300 μm pore-sized scaffolds for improved bone regeneration and repair.

4. Discussion

In this study, PCL scaffolds with specific pore sizes (100 μm, 200 μm, and 300 μm) were fabricated via EHD printing, and the effects of the pore sizes on macrophage polarization, FBR, immune microenvironment, and bone regeneration were comprehensively evaluated. The results showed that the 300 μm pore-sized scaffolds significantly promoted macrophage M2 polarization, decreased the expression of M1-related pro-inflammatory factors, improved the immune microenvironment at the bone defect site, and enhanced the generation and maturation of new bone under both *in vivo* and *in vitro* conditions. These findings underscore the potential of a 300 μm pore size as an optimal parameter in scaffold design for bone tissue regeneration.

There are inconsistent results in the literature regarding how different pore size materials regulate macrophage polarization.[21,22,45] Such differences may arise from variations in material fabrication methods, pore size designs, and scaffold geometrical characteristics. Specifically, the freeze-drying method used by Jiang *et al.*[21] yielded materials with irregular pore size distributions and limited control over pore uniformity, whereas the precision template–based approach used by Hady *et al.*[22] may also have been affected by slight deviations in pore size distribution. In the present study, the precise control of pore size was achieved using EHD printing technology, which significantly reduced the variable interference

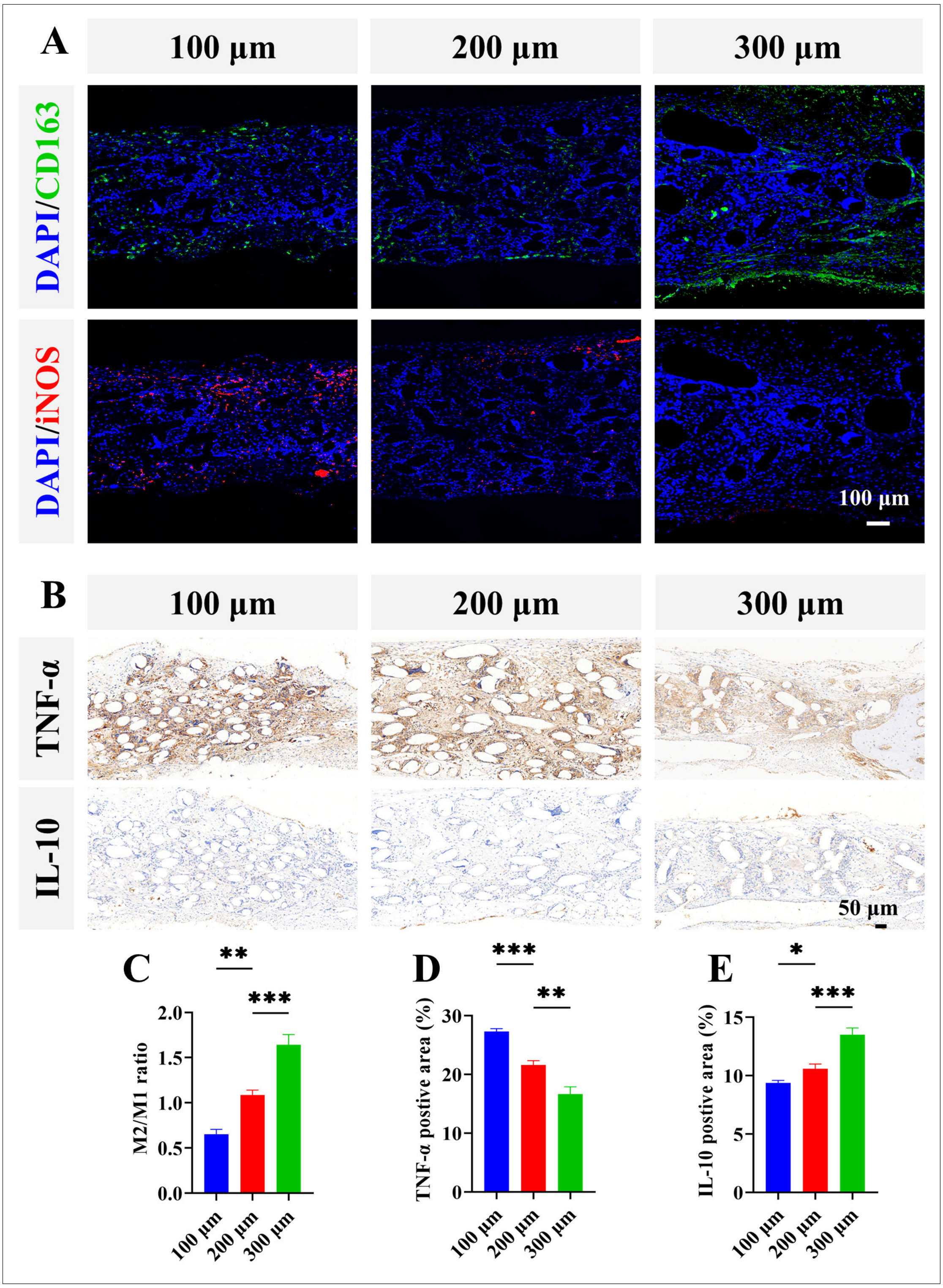

Figure 8. Effect of scaffolds with different pore sizes on macrophage phenotypic switching in a bone defect model. (A) Immunofluorescence staining images. Green indicates CD163 (M2 marker) and red indicates iNOS (M1 marker). Scale bars: 100 µm; magnifications: ×40. (B) Immunochemical staining images of TNF-α and IL-10. Scale bars: 50 µm; magnifications: ×40. (C) M2/M1 ratio and percentages of positive areas of (D) TNF-α and (E) IL-10 in the three groups of scaffolds. Notes: $n = 4$; $^{*}p < 0.05$, $^{**}p < 0.01$, $^{***}p < 0.001$. Abbreviations: CD163, cluster of differentiation 163; IL-10, interleukin-10; iNOS, inducible nitric oxide synthase; TNF-α, tumor necrosis factor-alpha.

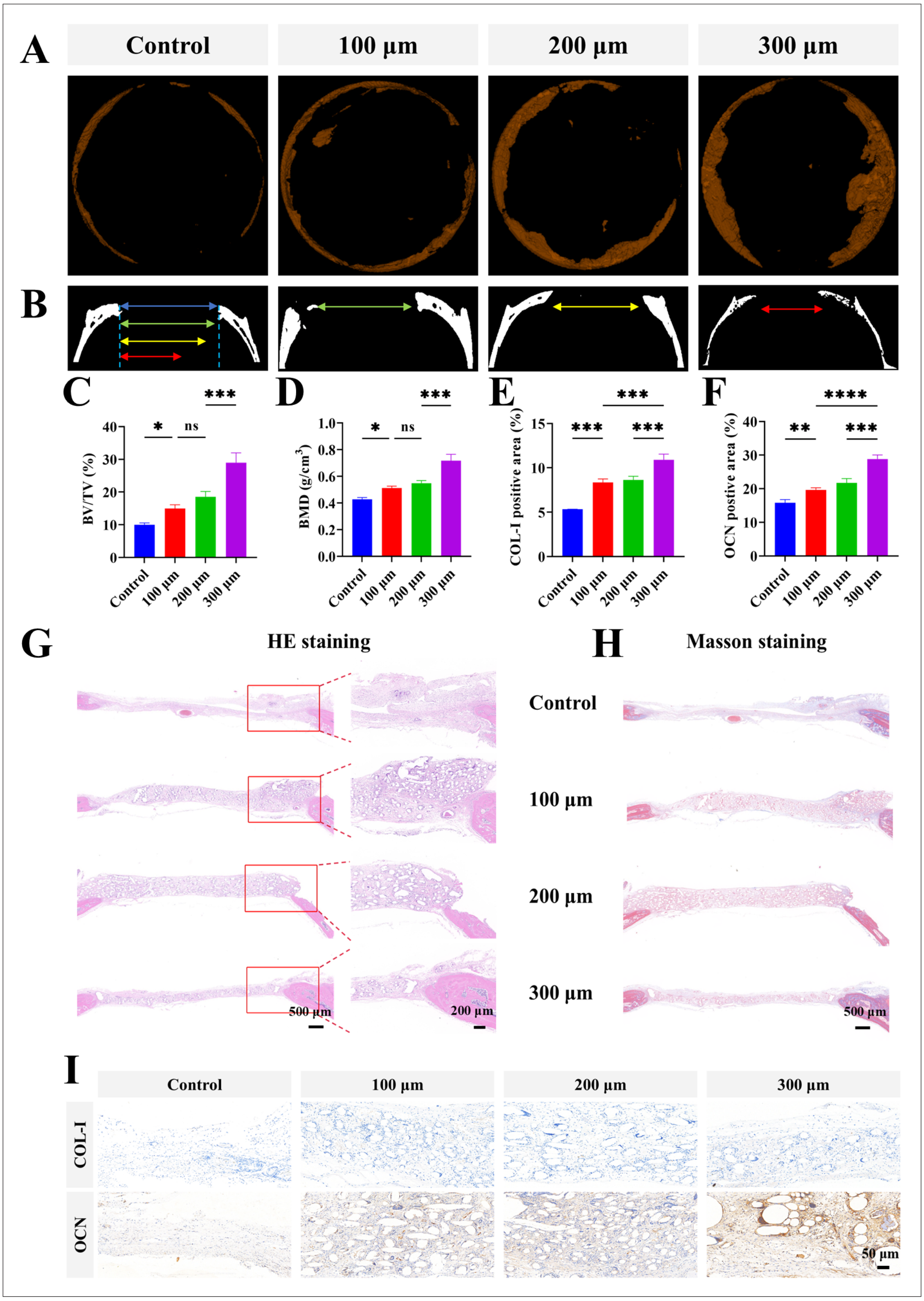

Figure 9. Bone regeneration in a rat cranial defect model treated with scaffolds of different pore sizes. (A) 3D reconstructed images of scaffolds in the four groups. (B) Sagittal positional images. Quantitative analysis results of (C) BV/TV, (D) BMD, and positive areas of (E) COL-I and (F) OCN in the four groups. (G) HE staining. Scale bars: (left) 500 μm, (right) 200 μm; magnifications: (left) ×4 , (right) ×10 . (H) Masson staining. Scale bars: 500 μm; magnifications: ×4. (I) Immunochemical staining of COL-I and OCN. Scale bars: 50 μm; magnifications: ×40. Notes: $n = 4$; $^{*}p < 0.05$, $^{**}p < 0.01$, $^{***}p < 0.001$, $^{****}p < 0.0001$. Abbreviations: BMD, bone mineral density; BV/TV, bone volume-to-tissue volume ratio; COL-I, collagen type-I; HE, hematoxylin–eosin; OCN, olsteocalcin.

due to uneven pore size. This enabled a more reliable demonstration of the promoting effect of the 300 μm pore size on macrophage M2 polarization and helped clarify, to a certain extent, the controversy regarding the relationship between scaffold pore size and macrophage polarization.

Additionally, compared with 100 μm and 200 μm pore sizes, the 300 μm pore size not only improved the spatial fitness of macrophages but also reduced the pro-inflammatory response triggered by high-density cell aggregation. Previous studies have shown that a larger pore size can provide a softer mechanical environment for macrophages by reducing the stiffness of the scaffold, thereby promoting their transition to the M2 phenotype.[40,46] In this study, simulation analysis and transcriptomic sequencing revealed that scaffold stiffness can regulate the direction of macrophage polarization by modulating the activation of the Piezo1 protein. In addition, scaffolds with larger pore sizes typically have improved breathability and nutrient supply, providing a more favorable growth environment for macrophages. This promotes their polarization toward the M2 type in relatively mild environments, thereby enhancing anti-inflammatory and tissue repair effects.[17] Moreover, the 300 μm pore-sized scaffolds promoted an M1-to-M2 phenotypic shift, as evidenced by a distinct cytokine profile (TNF-α, IL-6, IL-10, and TGF-β), fostering a pro-regenerative immune microenvironment. In *in vivo* experiments, the open structure of the 300 μm pore-sized scaffold enhanced angiogenesis, which is critical for immune modulation and bone regeneration. Neovascularization provided increased oxygen and nutrients, mitigating the detrimental effects of the hypoxic environment on macrophage phenotype and supporting their dynamic shift toward an anti-inflammatory phenotype. Furthermore, angiogenesis provided a favorable circulatory environment for osteoblast recruitment and differentiation, further enhancing local bone repair.

Previous studies have indicated that scaffolds with smaller pore sizes are more prone to eliciting an FBR.[47–50] This is attributed to the limited porosity of the scaffold surface, which leads to the sustained accumulation of pro-inflammatory macrophages and multinucleated giant cells. For example, Ivanova *et al.*[51] found that scaffolds with pore sizes less than 56 μm were more likely to induce fibrous capsule formation. Consistently, the results of this study showed that a 300 μm pore size significantly reduced the occurrence of FBR. In the *in vivo* implantation experiments, a large number of multinucleated FBGCs and thick fibrous capsule formation were observed on the surface of the scaffolds in the 100 μm and 200 μm groups. In contrast, the 300 μm group not only significantly reduced the aggregation of FBGCs but also suppressed the chronic inflammatory response by upregulating the expression of the anti-inflammatory factor IL-10. Further analysis revealed that the fibrous capsule thickness in the 300 μm group was significantly lower than that in the other two groups, accompanied by increased neovascularization and reduced inflammatory cell infiltration. These results suggest that the 300 μm pore-sized scaffold can significantly reduce the FBR by regulating macrophage phenotype switching and reducing pro-inflammatory signaling, thereby enhancing the biocompatibility of the material.

Macrophage phenotype plays a key role in bone regeneration.[52–55] In this study, we achieved precise control of pore size through EHD printing and established a causal link between macrophage phenotype, scaffold pore size, and osteogenic differentiation. The 300 μm group not only increased the M2/M1 ratio of macrophages but also potently activated the expression of osteogenic markers (*Runx2*, *Col1*, and *Ocn*), highlighting pore size as a critical parameter orchestrating the coupling between immunomodulation and osteogenesis. In *in vivo* experiments, the 300 μm group showed significant increases in BV/TV and BMD, even though the magnitude of the increase was not pronounced. Such moderate yet significant enhancement is reasonable for a cell-free scaffold without any osteoinductive factors, where substantial bone formation is generally limited. Moreover, histological and morphological analyses revealed clearer pore size-dependent differences in tissue infiltration, vascular-like structures, and osteoid deposition. These results indicate that macrophage polarization synergizes with osteogenesis temporally and spatially, and the 300 μm scaffold optimizes the dynamic balance in this process.

Despite the remarkable results of this study, some limitations exist. First, only PCL was selected as the matrix material, and its biocompatibility and degradation behavior may limit the broad applicability of the results. Future studies should incorporate multicomponent composites, such as hydroxyapatite and collagen, to verify the generalizable effect of pore size on different materials. Second, the experiments were primarily based on a rat model, which, despite providing important *in vivo* data, has an immune system that differs from that of humans. Therefore, further validation using large animal models or clinical trials is necessary to enhance translational potential. Future research could also focus on the development of personalized scaffold design solutions using artificial intelligence techniques to comprehensively optimize the pore size, shape, and mechanical properties of scaffolds, thereby providing more precise solutions for bone regeneration. Furthermore, research should explore the effects of scaffold structure on other immune cells, such as T cells, B cells, and dendritic cells, to gain a more comprehensive understanding of immune responses in tissue regeneration.

5. Conclusion

In this study, PCL scaffolds with varying pore sizes (100 µm, 200 µm, and 300 µm) were fabricated using EHD printing, and their modulatory effects on macrophage polarization, the immune microenvironment, and bone regeneration were systematically elucidated. Scaffolds with a 300 µm pore size significantly improved the local immune microenvironment by driving macrophage polarization toward the M2 phenotype, enhancing anti-inflammatory factor expression, suppressing pro-inflammatory mediators, and promoting angiogenesis. Furthermore, simulation analysis and transcriptomics sequencing indicated that pore size regulates macrophage Piezo1 activation by influencing scaffold stiffness, thereby affecting the polarization process. Moreover, scaffolds with a 300 µm pore size significantly alleviated the FBR, enhanced the expression of osteogenic genes and mineralized matrix deposition, and promoted new bone formation and tissue maturation both *in vitro* and *in vivo*. This study clarifies the superiority of 300 µm pore size in PCL scaffold design, provides an important basis for promoting bone regeneration through immunomodulation, and offers scientific evidence to support the development and clinical translation of high-performance tissue engineering scaffolds.

Acknowledgments

None.

Funding

This work was financially supported by the National Key R&D Program of China (No. 2024YFB4607800), the National Natural Science Foundation of China (52125501, 52405325, 82072522), the Cross training Support Project for Doctoral Students at Xi'an Jiaotong University (IDT2315), the Key Research Project of Shaanxi Province (2021LLRH-08), the Program for Innovation Team of Shaanxi Province (2023-CX-TD-17), the Postdoctoral Fellowship Program of CPSF (GZB20230573), the Postdoctoral Project of Shaanxi Province (2023BSHYDZZ30), and the Fundamental Research Funds for the Central Universities (xzy012023022).

Conflict of interest

Jiankang He serves as the Editorial Board Member of the journal, but did not in any way involve in the editorial and peer-review process conducted for this paper, directly or indirectly. Other authors declare they have no competing interests.

Author contributions

Funding acquisition: Wei Wang, Jiankang He
Investigation: Junzheng Liu, Jiahao Zhang
Methodology: Junzheng Liu, Jiaming Yu, Qin Guo, Yulin Wang, Jiahao Zhang
Resources: Jiankang He
Software: Junzheng Liu, Jiaming Yu, Le Jia
Validation: Zijie Meng, Qin Guo, Wei Wang
Writing–original draft: Junzheng Liu, Zijie Meng
Writing–review and editing: Wei Wang, Jiankang He

Ethics approval and consent to participate

The animal study was approved by the Ethics Committees of Xi'an Jiaotong University (2020-752).

Consent for publication

Not applicable.

Availability of data

The raw data underlying this study are available from the corresponding author upon reasonable request.

References

1. Liu L, Chen H, Zhao X, *et al*. Advances in the application and research of biomaterials in promoting bone repair and regeneration through immune modulation. *Mater Today Bio*. 2024;30:101410. doi: 10.1016/j.mtbio.2024.101410
2. Szczodra A, Houaoui A, Agniel R, *et al*. Boron substitution in silicate bioactive glass scaffolds to enhance bone differentiation and regeneration. *Acta Biomater*. 2024;186:489-506. doi: 10.1016/j.actbio.2024.07.053
3. He X, Liu Y, Dai Z *et al*. Yoda1 pretreated BMSC derived exosomes accelerate osteogenesis by activating phospho-ErK signaling via Yoda1-mediated signal transmission. *J Nanobiotechnol*. 2024;22(1):407. doi: 10.1186/s12951-024-02669-0
4. Dang Y, Zhang Y, Luo G, *et al*. The decisive early phase of biomaterial-induced bone regeneration. *Appl Mater Today*. 2024;38:102236. doi: 10.1016/j.apmt.2024.102236
5. Jin S, Wen J, Zhang Y, *et al*. M2 macrophage-derived exosome-functionalized topological scaffolds regulate the foreign body response and the coupling of angio/osteoclasto/osteogenesis. *Acta Biomater*. 2024;177:91-106. doi: 10.1016/j.actbio.2024.01.043

6. Qiu D, Cao C, Prasopthum A, *et al*. Elucidating osseointegration in vivo in 3D printed scaffolds eliciting different foreign body responses. *Mater Today Bio*. 2023;22:100771.
doi: 10.1016/j.mtbio.2023.100771
7. Mesa-Restrepo A, Byers E, Brown JL, Ramirez J, Allain JP, Posada VM. Osteointegration of Ti bone implants: a study on how surface parameters control the foreign body response. *ACS Biomater Sci Eng*. 2024;10(8):4662-4681.
doi: 10.1021/acsbiomaterials.4c00114
8. Dondossola E, Holzapfel BM, Alexander S, Filippini S, Hutmacher DW, Friedl P. Examination of the foreign body response to biomaterials by nonlinear intravital microscopy. *Nat Biomed Eng*. 2016;1:0007.
doi: 10.1038/s41551-016-0007
9. Anderson JM, Rodriguez A, Chang DT. Foreign body reaction to biomaterials. *Semin Immunol*. 2008;20(2):86-100.
doi: 10.1016/j.smim.2007.11.004
10. Fu M, Yang C, Sun G. Recent advances in immunomodulatory hydrogels biomaterials for bone tissue regeneration. *Mol Immunol*. 2023;163:48-62.
doi: 10.1016/j.molimm.2023.09.010
11. Li W, Dai F, Zhang S, *et al*. Pore size of 3D-printed polycaprolactone/polyethylene glycol/hydroxyapatite scaffolds affects bone regeneration by modulating macrophage polarization and the foreign body response. *ACS Appl Mater Interfaces*. 2022;14(18):20693-20707.
doi: 10.1021/acsami.2c02001.
12. Franz S, Rammelt S, Scharnweber D, Simon JC. Immune responses to implants - a review of the implications for the design of immunomodulatory biomaterials. *Biomaterials*. 2011;32(28):6692-6709.
doi: 10.1016/j.biomaterials.2011.05.078.
13. Kastellorizios M, Papadimitrakopoulos F, Burgess DJ. Multiple tissue response modifiers to promote angiogenesis and prevent the foreign body reaction around subcutaneous implants. *J Control Release*. 2015;214:103-111.
doi: 10.1016/j.jconrel.2015.07.021.
14. Spiller KL, Nassiri S, Witherel CE, *et al*. Sequential delivery of immunomodulatory cytokines to facilitate the M1-to-M2 transition of macrophages and enhance vascularization of bone scaffolds. *Biomaterials*. 2015;37:194-207.
doi: 10.1016/j.biomaterials.2014.10.017.
15. Li R, Zhang K, Dong C, Wang K, Gu X, Qin Y. Osteoinductivity enhancement by tailoring the surface chemical bond status: a strategy to mobilize host bone growth factors for in situ bone regeneration. *Mater Today Bio*. 2024;29:101256.
doi: 10.1016/j.mtbio.2024.101256.
16. Vegas AJ, Veiseh O, Doloff JC, *et al*. Combinatorial hydrogel library enables identification of materials that mitigate the foreign body response in primates. *Nat Biotechnol*. 2016;34(6):345-352.
doi: 10.1038/nbt0616-666e.
17. Xiong S, Zhang Y, Zeng J, *et al*. DLP fabrication of HA scaffold with customized porous structures to regulate immune microenvironment and macrophage polarization for enhancing bone regeneration. *Mater Today Bio*. 2024;24:100929.
doi: 10.1016/j.mtbio.2023.100929.
18. Veiseh O, Doloff JC, Ma M, *et al*. Size- and shape-dependent foreign body immune response to materials implanted in rodents and non-human primates. *Nat Mater*. 2015;14(6):643–651.
doi: 10.1038/nmat4290.
19. Sridharan R, Cavanagh B, Cameron AR, Kelly DJ, O'Brien FJ. Material stiffness influences the polarization state, function and migration mode of macrophages. *Acta Biomater*. 2019;89:47-59.
doi: 10.1016/j.actbio.2019.02.048.
20. Xia D, Wang Y, Wu R, *et al*. The effect of pore size on cell behavior in mesoporous bioglass scaffolds for bone regeneration. *Appl Mater Today*. 2022;29:101607.
doi: 10.1016/j.apmt.2022.101607
21. Jiang S, Lyu C, Zhao P, *et al*. Cryoprotectant enables structural control of porous scaffolds for exploration of cellular mechano-responsiveness in 3D. *Nat Commun*. 2019;10(1):3491.
doi: 10.1038/s41467-019-11397-1.
22. Hady TF, Hwang B, Pusic AD, *et al*. Uniform 40-µm-pore diameter precision templated scaffolds promote a pro-healing host response by extracellular vesicle immune communication. *J Tissue Eng Regen Med*. 2020; 15(1):24-36.
doi: 10.1002/term.3160.
23. Meng Z, Yang S, Yin F, *et al*. 3D-printed biodegradable polycaprolactone rib implants with tissue-specific mechanical properties promote chest wall recovery by stimulating tissue fibrosis. *Virtual Phys Prototyp*. 2024;19(1):2346816.
doi: 10.1080/17452759.2024.2346816.
24. He J, Xia P, Li D. Development of melt electrohydrodynamic 3D printing for complex microscale poly (ε-caprolactone) scaffolds. *Biofabrication*. 2016;8(3):035008.
doi: 10.1088/1758-5090/8/3/035008.
25. Han K, He J, Fu L, Mao M, Kang Y, Li D. Engineering highly-aligned three-dimensional (3D) cardiac constructs for enhanced myocardial infarction repair. *Biofabrication*. 2022;15(1):015003.
doi: 10.1088/1758-5090/ac94f9.
26. Shi Y, Wang L, Sun L, *et al*. Melt electrospinning writing PCL scaffolds after alkaline modification with outstanding cytocompatibility and osteoinduction. *Int J Bioprint*. 2023;9(6):1071.
doi: 10.36922/ijb.1071.
27. Yao C, Qiu Z, Li X, Zhu H, Li D, He J. Electrohydrodynamic printing of microfibrous architectures with cell-scale spacing

for improved cellular migration and neurite outgrowth. *Small.* 2023;19(19):2207331.
doi: 10.1002/smll.202207331.

28. Tylek T, Blum C, Hrynevich A, *et al*. Precisely defined fiber scaffolds with 40 µm porosity induce elongation driven M2-like polarization of human macrophages. *Biofabrication.* 2020;12(2):025007.
doi: 10.1088/1758-5090/ab5f4e.

29. Bružauskaitė I, Bironaitė D, Bagdonas E, Bernotienė E. Scaffolds and cells for tissue regeneration: different scaffold pore sizes—different cell effects. *Cytotechnology.* 2016;68(3):355-369.
doi: 10.1007/s10616-015-9895-4.

30. Zhang Y, Li R, Wu W, *et al*. Adhesion and proliferation of osteoblast-like cells on porous polyetherimide scaffolds. *Biomed Res Int.* 2018;2018:1491028.
doi: 10.1155/2018/1491028.

31. Lai Y, Cao H, Wang X, *et al*. Porous composite scaffold incorporating osteogenic phytomolecule icariin for promoting skeletal regeneration in challenging osteonecrotic bone in rabbits. *Biomaterials.* 2017;153:1-13.
doi: 10.1016/j.biomaterials.2017.10.025.

32. Hu S, Meng Z, Zhou J, *et al*. Enhanced attachment and collagen type I deposition of MC3T3-E1 cells via electrohydrodynamic printed sub-microscale fibrous architectures. *Int J Bioprint.* 2022;8(2):514.
doi: 10.18063/ijb.v8i2.514.

33. Brennan CM, Eichholz KF, Hoey DA. The effect of pore size within fibrous scaffolds fabricated using melt electrowriting on human bone marrow stem cell osteogenesis. *Biomed Mater.* 2019;14(6):065016.
doi: 10.1088/1748-605x/ab49f2.

34. Shi Y, Tao W, Yang W, *et al*. Calcium phosphate coating enhances osteointegration of melt electrowritten scaffold by regulating macrophage polarization. *J Nanobiotechnol.* 2024;22(1):47.
doi: 10.1186/s12951-024-02310-0.

35. Palmieri EM, McGinity C, Wink DA, McVicar DW. Nitric oxide in macrophage immunometabolism: hiding in plain sight. *Metabolites.* 2020;10(11):429.
doi: 10.3390/metabo10110429.

36. Zhao DW, Liu C, Zuo KQ, *et al*. Strontium-zinc phosphate chemical conversion coating improves the osseointegration of titanium implants by regulating macrophage polarization. *Chem Eng J.* 2020;408:127362.
doi: 10.1016/j.cej.2020.127362.

37. Lv L, Xie Y, Li K, *et al*. Unveiling the mechanism of surface hydrophilicity-modulated macrophage polarization. *Adv Healthc Mater.* 2018;7(19):1800675.
doi: 10.1002/adhm.201800675.

38. Abedin E, Lari R, Mahdavi Shahri N, Fereidoni M. Development of a demineralized and decellularized human epiphyseal bone scaffold for tissue engineering: a histological study. *Tissue Cell.* 2018;55:46-52.
doi: 10.1016/j.tice.2018.09.003.

39. Wei X, Zhou W, Tang Z, *et al*. Magnesium surface-activated 3D printed porous PEEK scaffolds for in vivo osseointegration by promoting angiogenesis and osteogenesis. *Bioact Mater.* 2023;20:16-28.
doi: 10.1016/j.bioactmat.2022.05.011.

40. Xu J, Guan W, Kong Y, *et al*. Regulation of macrophage behavior by chitosan scaffolds with different elastic modulus. *Coatings.* 2022;12(11):1742.
doi: 10.3390/coatings12111742.

41. Du Y, Xu B, Li Q, Peng C, Yang K. The role of mechanically sensitive ion channel Piezo1 in bone remodeling. *Front Bioeng Biotechnol.* 2024;12:1342149.
doi: 10.3389/fbioe.2024.1342149.

42. Li W, Xu F, Dai F, *et al*. Hydrophilic surface-modified 3D printed flexible scaffolds with high ceramic particle concentrations for immunopolarization-regulation and bone regeneration. *Biomater Sci.* 2023;11:3976-3997.
doi: 10.1039/d3bm00362k.

43. Mahon OR, Browe DC, Gonzalez-Fernandez T, *et al*. Nano-particle mediated M2 macrophage polarization enhances bone formation and MSC osteogenesis in an IL-10 dependent manner. *Biomaterials.* 2020;239:119833.
doi: 10.1016/j.biomaterials.2020.119833.

44. Li Y, He J, Zhou J, *et al*. A conductive photothermal non-swelling nanocomposite hydrogel patch accelerating bone defect repair. *Biomater Sci.* 2022;10:1326-1341.
doi: 10.1039/d1bm01937f.

45. Garg K, Pullen NA, Oskeritzian CA, Ryan JJ, Bowlin GL. Macrophage functional polarization (M1/M2) in response to varying fiber and pore dimensions of electrospun scaffolds. *Biomaterials.* 2013;34(18):4439-4451.
doi: 10.1016/j.biomaterials.2013.02.065.

46. Yin Y, He XT, Wang J, *et al*. Pore size-mediated macrophage M1-to-M2 transition influences new vessel formation within the compartment of a scaffold. *Appl Mater Today.* 2019;18:100466.
doi: 10.1016/j.apmt.2019.100466.

47. Sridharan R, Cameron AR, Kelly DJ, Kearney CJ, O'Brien FJ. Biomaterial based modulation of macrophage polarization: a review and suggested design principles. *Mater Today.* 2015;18(6):313-325.
doi: 10.1016/j.mattod.2015.01.019.

48. Zhang D, Chen Q, Shi C, *et al*. Dealing with the foreign-body response to implanted biomaterials: strategies and applications of new materials. *Adv Funct Mater.* 2021;31(6):2007226.

doi: 10.1002/adfm.202007226.

49. Liu Y, Suarez-Arnedo A, Riley L, Miley T, Xia J, Segura T. Spatial confinement modulates macrophage response in microporous annealed particle (MAP) scaffolds. *Adv Healthcare Mater.* 2023;12(26):2300823.
doi: 10.1002/adhm.202300823.

50. Sheikh Z, Brooks P, Barzilay O, Fine N, Glogauer M. Macrophages, foreign body giant cells and their response to implantable biomaterials. *Materials.* 2015;8(9):5671-5701.
doi: 10.3390/ma8095269

51. Ivanova E, Fayzullin A, Minaev N, *et al*. Surface topography of PLA implants defines the outcome of foreign body reaction: an in vivo study. *Polymers*. 2023;15(20):4119.
doi: 10.3390/polym15204119.

52. Zhao SJ, Kong FQ, Jie J, *et al*. Macrophage MSR1 promotes BMSC osteogenic differentiation and M2-like polarization by activating PI3K/AKT/GSK3β/β-catenin pathway. *Theranostics*. 2020;10(1):17-35.
doi: 10.7150/thno.36930.

53. Fan S, Zhang C, Sun X, *et al*. Metformin enhances osteogenic differentiation of BMSC by modulating macrophage M2 polarization. *Sci Rep*. 2024;14(1):20267.
doi: 10.1038/s41598-024-71318-1.

54. Feito MJ, Casarrubios L, Oñaderra M, *et al*. Response of RAW 264.7 and J774A.1 macrophages to particles and nanoparticles of a mesoporous bioactive glass: a comparative study. *Colloids Surf B Biointerfaces.* 2021;208:112110.
doi: 10.1016/j.colsurfb.2021.112110

55. Trentini M, D'Amora U, Ronca A, *et al*. Bone regeneration revolution: pulsed electromagnetic field modulates macrophage-derived exosomes to attenuate osteoclastogenesis. *Int J Nanomed*. 2024;19:8695-8707.
doi: 10.2147/ijn.s470901.